Medical Image Analysis xxx (2008) xxx–xxx

Contents lists available at ScienceDirect

Medical Image Analysis

journal homepage: www.elsevier.com/locate/media

Fusion of optical imaging and MRI for the evaluation and adjustment of macroscopic models of cardiac electrophysiology: A feasibility study

Mihaela Pop [a,*], Maxime Sermesant [b,c], Damien Lepiller [b], Michael V. Truong [a], Elliot R. McVeigh [d], Eugene Crystal [e], Alexander Dick [f], Herve Delingette [b], Nicholas Ayache [b], Graham A. Wright [a]

[a] Department of Medical Biophysics, University of Toronto, Sunnybrook Health Sciences Centre, Imaging Research, 2075 Bayview Avenue, Room S612, Toronto, ON, Canada M4N 3M5
[b] ASCLEPIOS Project, INRIA, Sophia Antipolis, France
[c] Division of Imaging Science, King's College, London, UK
[d] Johns Hopkins University, Baltimore, MD, USA
[e] Arrhythmia Services, Sunnybrook Health Sciences Centre, Toronto, Canada
[f] Department of Cardiology, University of Toronto, Sunnybrook Health Sciences Centre, 2075 Bayview Avenue, Toronto, ON, Canada M4N 3M5

ARTICLE INFO

Article history:
Received 6 February 2008
Received in revised form 10 July 2008
Accepted 16 July 2008
Available online xxxx

Keywords:
Computer modelling
Electrophysiology
Optical imaging
MRI

ABSTRACT

The aim of this work was to demonstrate the correspondence between a macroscopic 3D computer model of electrophysiology (i.e., the Aliev–Panfilov model) parametrized with MR data and experimental characterization of action potential propagation in large porcine hearts, *ex vivo*, using optical methods (based on voltage-sensitive fluorescence). A secondary goal was to use one of these studies to demonstrate an optimized method for regional adjustment of critical model parameters (i.e., adjustment of the local conductivity from the isochronal maps obtained via optical images). There was good agreement between model behaviour and experiment using fusion of optical and MR data, and model parameters from previous work in the literature. Specifically, qualitative comparison between computed and measured activation maps gave good results. Adjustment of the conductivity parameter within 26 regions fitting data from the current experiments in one heart reduced absolute error in local depolarization times by a factor of 3 (i.e. from 30 to 10 ms).

1. Introduction

Computer modelling is a powerful tool used in cardiac electrophysiology to predict the electrical activity in normal and pathologic hearts. In particular, it could help us understand and predict the arrhythmic events associated with myocardial infarction, a major cause of deaths (Kleber and Rudy, 2004). Detailed ionic models, as well as macroscopic, phenomenological models have been proposed in computational electrophysiology to solve for the action potential (AP) propagation and its duration (Clayton and Holden, 2004, 2005; Aliev and Panfilov, 1996a,b; Nash and Panfilov, 2004). The specific mathematical approach is usually chosen by investigators based on the available input and desired output parameters, as well as computational resources. For example, the two-variable monodomain model developed by Aliev and Panfilov (based on reaction–diffusion equations) solves for the action potential without computing ionic currents (Aliev and Panfilov, 1996b). This macroscopic model was implemented recently by Sermesant et al. (2005, 2006) who developed an electromechanical cardiac model feasible for use in characterizing action potential propagation in large hearts with computational times on the order of 1 h to model one heartbeat (on one PC compared to more than 30 processors used in ionic or bidomain models); this makes it attractive for clinical applications (i.e., diagnosis and treatment planning). Moreover, efforts are being made to further simplify the monodomain equations with eikonal equations (Keener and Sneyd, 1998), and compute even more rapidly the spread of excitation and associated patterns. Though extremely attractive for clinical implementation, the utility and accuracy of theoretical predictions of such fast macroscopic models require experimental confirmation; and likely, some tuning of the model parameters will be necessary to characterize model behaviour with sufficient accuracy for certain clinical applications.

It is, however, very challenging to non-invasively obtain physiological measurements at adequate temporal and spatial resolution for comparison with the output of the models using data that reflects *in vivo* geometry and physiology. For instance, to calculate the duration of the action potential, one needs the precise depolarization and repolarization times. Currently, monophasic action potentials (MAP) can be recorded *in vivo* via a catheter electrode inserted into the heart; however, this electrode records

* Corresponding author. Tel.: +1 416 4806100x3392.
E-mail address: mpop@sri.utoronto.ca (M. Pop).

1361-8415/$ - see front matter © 2008 Elsevier B.V. All rights reserved.
doi:10.1016/j.media.2008.07.002

only one measurement, from the location where it is positioned (Kim et al., 2002; Hao et al., 2004); this limits the number of measures that can be made since they are obtained under fluoroscopy. To increase the number of simultaneous recordings *in vivo*, one can obtain surfacic measurements using either a catheter basket (which does not touch the endocardium but rather floats in the blood cavity) (Eldar et al., 1997; Schmitt et al., 1999), or an electrode-sock (comprising 256 or more electrodes), which has excellent temporal resolution but records only the extracellular potentials on the epicardial surface (Bayly et al., 1998; Ciaccio and Lee, 2002; Faris et al., 2003). Sermesant et al. (2003) showed preliminary results in integrating such surfacic data into a surfacic model, though a 3D volumetric model should be more appropriate. Controlled experiments can also be performed *ex vivo*; for example, in a recent study by Taccardi et al. (2008) simultaneous epicardial and intramural recordings were obtained in canine hearts *ex vivo*, improving our understanding of the ventricle excitation under controlled ventricular pacing and providing proof that epicardial excitation has heterogeneous propagation velocities due to the architecture of myocardial muscle. However, the epicardial and intramural recording electrodes can damage the muscle, making difficult a subsequent determination of the fiber directions.

An alternative is given by an optical imaging technique, which has been shown to provide fast and accurate measurements of AP in explanted normal and diseased hearts prepared under physiological conditions approximating those *in vivo* (Efimov et al., 2004; Kay et al., 2004; Banville and Gray, 2002; Yang et al., 2007). The technique uses a fluorescence dye which is sensitive to the changes in transmembrane potential. With this, the changes in signal intensity reflecting AP can be recorded optically at submillimetre spatial resolution and high temporal resolution (1–3.7 ms) from the exposed surface (1 ms being desirable when mapping fibrillation and small hearts, because they are characterized by short heart cycles). A potential drawback of the technique is that it makes use of an electro-mechanical uncoupler (e.g., DAM, BDM, cytochalasin) to avoid motion artifacts, which could slightly change the AP duration compared to *in vivo* physiological values; however, recent studies suggest these changes are small (Qin et al., 2003). The technique is not feasible in humans due to the toxicity of dye, though, in a collaborative study, we demonstrated the feasibility of optically mapping normal propagation and ventricular fibrillation on the endocardium and epicardium of explanted cardiomyopathic human hearts (Nanthakumar et al., 2007). Progress has also been made to facilitate relating optical experiments to theoretical models, correcting the interpretation of optical signals hampered by the fluorescent photon scattering in rabbit hearts and slab tissues (Bishop et al., 2006; Hyatt et al., 2005). In addition, to avoid erroneous estimations of conduction velocity, a few methods have also been proposed to reconstruct the 3D heart surface from 2D optical images (Sung et al., 2000; Kay et al., 2004; Chung et al., 2006).

However, for theoretical models with sufficient accuracy to reflect physiological behavior, the anisotropy introduced by the fibers also has to be determined with sufficient spatial resolution (Kadish et al., 1988; Vetter et al., 2005). Often this is determined from histology, an invasive, laborious procedure. Diffusion-weighted magnetic resonance (MR) imaging is an alternative, which can be used to reconstruct the fiber directions with high spatial resolution, particularly for *ex vivo* preparations (Helm et al., 2005).

A 3D macroscopic model suitable for clinical applications, has to be first tested under controlled conditions. To mimic the clinical situation (where surfacic measurements would be registered with a 3D volumetric model), we start with an *ex vivo* experiment in a large heart model, and optically map the electrical activation on the epicardium. From comparisons between measured and computed activation maps (initialized with data from literature), one can further proceed with finer, regional tuning of the model parameters (e.g., local conductivity). The regional tuning would be very useful in clinical applications since it could for instance provide maps of conductivity. Such maps are very useful if one needs to differentiate between infarct scars and normal myocardium.

In this paper, we present results comparing experimental studies in explanted healthy porcine hearts with the Aliev and Panfilov monodomain model. Specifically, the first aim was to compare measured maps of epicardial activity with theoretical predictions from a model calibrated to the experimental situation. In accordance with Fig. 1, we include qualitative comparison of the measured and computed activation maps, observing the model's response to different pacing frequencies as well as to stimulations from different sites. The model is built by fusing optical imaging and MRI. Although multiple hearts were used during this study (see summary in Table 1), throughout the paper we show examples primarily from one heart. A second goal was to demonstrate the potential for customization of such models to better reflect experimentally demonstrated model behaviour, for instance through the adjustment of regional model parameters determining conductivity and AP propagation velocity from the isochronal maps.

2. Methodology

In this section, we describe in detail the steps performed to build the validation framework proposed above. We first performed the optical experiment, and then used MR imaging to

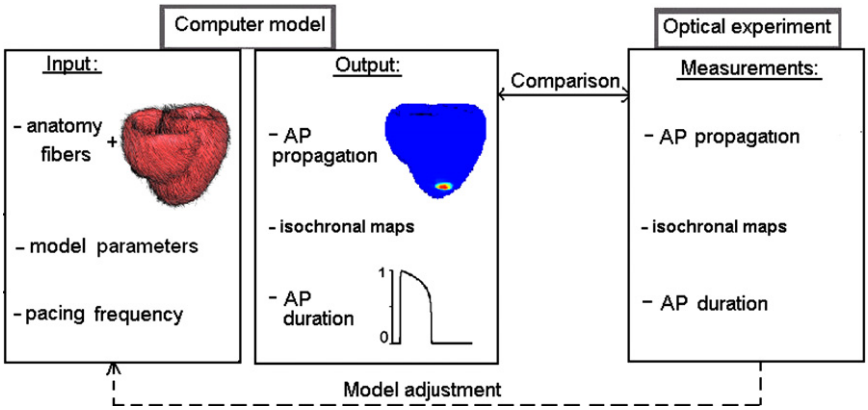

Fig. 1. Diagram for the comparisons between the theoretical predictions of the model generated from MRI and the optical measurements.

Table 1
Summary of the experiments detailing what was performed (or not) in each heart

Heart number	Stereo reconstruction	MRI – DTI fibers	Average distance between markers from camera image and from MRI volume considered for Horn's calculation	Multiple frequencies	Multiple pacing sites
1	Yes	No	NA	No (only 1.2 Hz)	No
2	No	No	NA	No (only 1.2 Hz)	No
3	Yes	Yes	2.6 mm	No	No
4	Yes	Yes	1.2 mm	Yes	No
5	Yes	Yes	2.5 mm	No (only 1.1 Hz)	Yes (4 sites)
6	Yes	Yes	2.1 mm	No	No
7	Yes	Yes	1.5 mm	No (only 1.1 Hz)	Yes (3 sites)

In all hearts we obtained a good agreement between measured and simulated activation maps, however, the adjustment step was performed only for one heart (i.e., heart number 5).

construct the computer model (i.e., the anatomy and fiber directions) of the same heart. The computational mesh was constructed from the anatomy scans and the simulations were performed with parameters that reproduced exactly the experimental conditions (e.g., the position of pacing electrode, the duration of stimulus, etc).

2.1. Optical experiment

Swine weighing 20–25 kg were anesthetized, the chests opened, and the hearts exposed in accordance to the animal research protocol guidelines approved at Sunnybrook Health Sciences Centre, Toronto, Canada. The hearts (a total of seven included in this study, for various aims as summarized in Table 1) were immediately excised after euthanasia. The blood was flushed out and the aorta rapidly cannulated and attached to a Langendorff perfusion system. Throughout the experiments, the hearts were constantly perfused with a mixture of oxygenated blood and Tyrodes' solution (95% O_2 and 5% CO_2), maintained at a pH 7.3 ± 0.3 and at a temperature of 37.0 ± 0.5 °C. The hearts were paced via a bipolar stimulating $Ag/AgCl_2$ electrode (E) coated with gold at the tip to avoid polarization effects (GrassTelefactor, USA). The duration of the square-wave stimulus was set to 5 ms.

A 20-ml bolus of fluorescence dye solution (0.2 ml di4-ANEPPS, Biotium Inc.) was injected into the heart via the perfusion line for optical studies. To avoid motion artifacts, an electro-mechanical uncoupler (2,3-butanediome monoxime, Sigma–Aldrich) was also injected in the perfusate solution, resulting in suppression of the heart motion. The dye was excited with green light (530 ± 20 nm) via 150-W halogen lamps (MHF G150LR, Moritek Corp., Japan). To avoid photo-bleaching, the lamps were controlled by shutters (labeled 'S' in Fig. 2). The emitted signals from the hearts were filtered through a high-pass filter (>610 nm) and captured by a high-speed dual-CCD system (MICAM02, BrainVision Inc., Japan) with 3.76-ms temporal resolution. The field of view of 184×124 pixels (12×8 cm) yielded approximately 0.7-mm spatial resolution.

The relative changes in the intensity of the fluorescence follow the changes in transmembrane potential (see Fig. 3a, where red corresponds to the depolarization of the heart tissue and blue corresponds to the resting phase; the direction of wave propagation is from the apex toward the base).

Further analysis of the fluorescence signal was performed in Matlab to characterize the behavior of the restitution properties for the AP duration over larger regions of interest (ROI). The change in fluorescence signal during depolarization and repolarization phases, was analyzed in Matlab. The optical traces (waves) at each

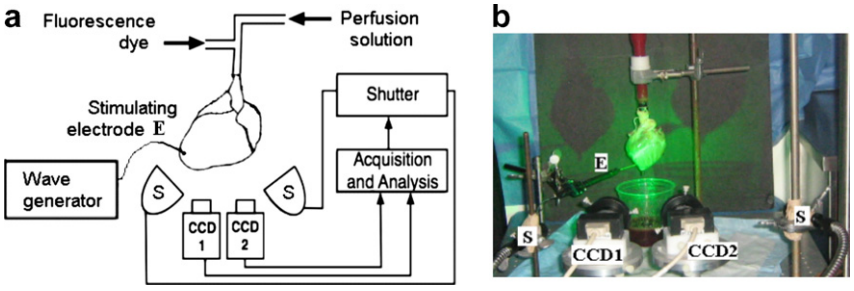

Fig. 2. Schematic of the optical experiment using a dual-camera system to record the action potential from the heart perfused *ex vivo* via a Langendorff system (a) and a snapshot of the actual experiment (b).

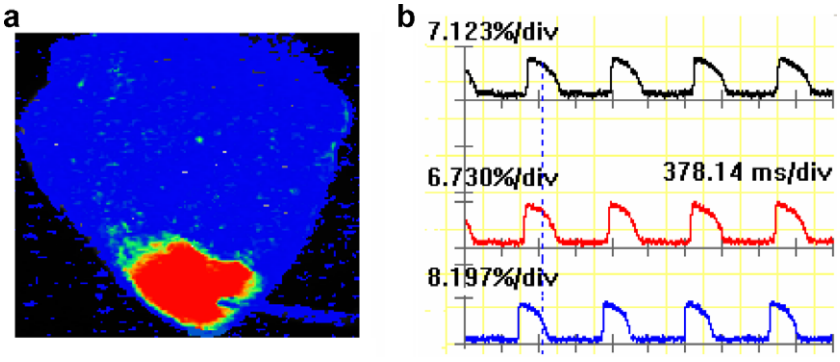

Fig. 3. (a) Loss of fluorescence signal reflects the changes in transmembrane potential such that we can visualize the depolarization wave (red) propagating through a heart (blue represents the resting phase); (b) examples of AP waves from different pixel locations caused by pacing at a frequency of 1.1 Hz. (For interpretation of the references to color in this figure legend, the reader is referred to the web version of this article.).

Please cite this article in press as: Pop, M. et al., Fusion of optical imaging and MRI for the evaluation and adjustment ..., Med. Image Anal. (2008), doi:10.1016/j.media.2008.07.002

pixel and the associated activation (depolarization time) and recovery (repolarization time) were detected using the first (dF/dt) and second (d^2F/dt^2) derivatives of the fluorescence signal intensity versus time. The APD_{90} (APD at 90% repolarization, which is 0.9 times the difference between the APD's peak amplitude and the baseline) was also calculated as per the method provided by Efimov et al. (1994).

The optical images recorded by the two CCD cameras were used to reconstruct the 3D surface of the heart. The details of the stereo reconstruction and calibration methods can be found elsewhere (Chung et al., 2006). Briefly, the stereo image pair under normal light conditions is used to generate disparity maps (left and right cameras) and the cameras' overlap yields the final reconstructed area. Camera calibration was performed in Matlab using the well-known Bouguet camera toolbox (details can be found here: http://www.vision.caltech.edu/bouguetj).

At the completion of the optical recordings, 5–7 opaque markers were glued onto the epicardium of different hearts to provide a way to register the optical images with the surface of the model generated from MR images (see below). We estimated a rigid transformation between the markers' optical and MR 3D coordinates by solving the least-squares difference using quaternions via a function implemented in Matlab libraries using Horn's algorithm (Horn, 1987). When pacing from the epicardial surface of the heart, one marker was placed at the location of the stimulating electrode and this location was specified in the simulations.

At the end of the optical experiment (before proceeding with the camera calibration described above), the blood perfusion line was switched to a formalin line and the hearts were continuously perfused with formalin (10%) for approximately 20 min. To ensure that no deformation of the hearts took place between the optical imaging and MR imaging experiments, the hearts were gently transferred and suspended in a container filled with formalin for preservation. Formalin is known to produce shrinkage of the tissue over weeks; however, we performed the MR imaging the following day so shrinkage should be negligible.

2.2. Magnetic resonance imaging

The ventricles were imaged using a 1.5 T Signa GE MR scanner for anatomy, fiber directions and markers locations. Just prior to MR imaging studies, we gently cut off the atria, large vessels and papillary muscle and placed the ventricles in a phantom box filled with fluorinert (which has negligible MR signal) for characterization of the fiber orientation; we subsequently re-filled the box with water to determine the marker coordinates. An affine registration was performed to align these two sets of images. For determining the marker locations on the heart we used a 3D fast spin echo (FSE) sequence using the following MR parameters: TE = 60 ms, TR = 1000 ms, slice thickness = 1.5 mm, a FOV and matrix yielding an in-plane interpolated resolution of 0.5×0.5 mm. The diffusion-weighted imaging sequence was developed at the Laboratory of Cardiac Energetics (NIH/NHLBI, USA) (Helm et al., 2005) and implemented on our research scanner. We used the following MR parameters: TE = 26 ms, TR=800 ms, NEX = 1, b-value = 700, 7 directions for diffusion gradients, with the same FOV/matrix as used in the FSE study. The heart anatomy was extracted from the un-weighted images (i.e., b = 0) and used to generate the volumetric mesh for the mathematical model.

2.3. Computer model

We use the Aliev and Panfilov model of the heart to perform our simulations, using the implementation detailed in (Sermesant et al., 2006) but with the restitution term included. In this model, described by the system of Eqs. (1) and (2), we solve for V, the action potential, and r, the recovery variable contribution:

$$\frac{\partial V}{\partial t} = \nabla \cdot (D \nabla V) - kV(V-a)(V-1) - rV + I_{\text{stim}}, \tag{1}$$

$$\frac{\partial r}{\partial t} = -\left(\varepsilon + \frac{\mu_1 r}{\mu_2 + V}\right)(ku(u-a-1) + r). \tag{2}$$

The term $-kV(V-a)(V-1)$ controls the fast processes (initiation and upstroke of action potential) via the threshold parameter a, while r, determines the dynamics of the repolarization phase. The term I_{stim} represents the extra stimuli (e.g., the pacing stimulus in the experiment). Most of the parameters (i.e., $\varepsilon = 0.01$ controlling the repolarization variable; $a = 0.1$ the threshold parameter; $k = 8$ controlling the reaction term; and $\mu_1 = 0.01$ and $\mu_2 = 0.3$ controlling the restitution curve) were set as in (Nash and Panfilov, 2004) to reproduce the shape, duration, and restitution of AP obtained from experiments in canine cardiac tissue, the only available data in the literature, given in (Elharrar and Surawicz, 1983). The model accounts for the heart anisotropy via the diffusion tensor, D, which depends on tissue diffusivity d (set to 1 for a normal/healthy conduction). In this model, the value of the anisotropy ratio is set to 0.25 for an electrical wave propagating twice as fast along the fiber as in the transverse direction. The variables in the model are dimensionless; therefore they must be re-scaled to be related to physical values. For example, the normalized AP in the model varies between 0 and 1, which corresponds to real values of transmembrane potential between −90 and +20 mV.

The heart surface mesh is created from the anatomical images using classical segmentation algorithms (thresholding, mathematical morphology, marching cubes) and then the volumetric tetrahedral mesh is generated with the GHS3D package (INRIA, France).

We solve for the transmembrane potential using the finite element method, with an explicit Euler time integration scheme. The code was written in C++ and uses OpenGL libraries to display the results. For the simulations presented in this study, we used a computational time step of 1×10^{-4} s. The simulation time for one heart cycle (of 0.85 s) on a mesh of approximately 75,000 elements is about 15 min on an Intel® Pentium 4, 3.2 GHz CPU, with 1 GB of RAM.

2.3.1. Model comparison with experiments and subsequent model adjustment

In order to evaluate the relevance of the model and its discretisation, we quantify the error between the simulations and the measurements. The mean error is calculated as the mean of the absolute value of the difference between the simulated depolarization times and the measured depolarization times (in ms) on the vertices where data is available.

To reduce the error, we examine here the effect of adjusting a pseudo-conductivity parameter which would reflect the differences in propagation velocity in the tissue. In the Aliev and Panfilov model, d and k are the main parameters involved in this propagation velocity. d represents the diffusion properties of the myocardial tissue (mainly gap junctions), whereas k accounts for the opening of the ionic channels, the reaction of the tissue to the depolarization. Both parameters can represent the variations of the propagation velocity in the tissue; low values for either parameter increase resistance to the propagation of the depolarization front, slowing the wavefront speed. As we only need one measure to adjust this speed, we chose to adjust locally the value of the parameter d, which will represent this pseudo-conductivity, while keeping k as a global constant.

The depolarization speed vector can be computed per triangle as the inverse of the gradient of the depolarization times of this triangle. This can be determined with standard linear shape functions

Please cite this article in press as: Pop, M. et al., Fusion of optical imaging and MRI for the evaluation and adjustment ..., Med. Image Anal. (2008), doi:10.1016/j.media.2008.07.002

already used for the Finite Element-based simulation, but it yields to discontinuous estimates of the local speed due to the noise in the measurement process. Thus, we average this estimate using the directly neighboring triangles. Simulated speed along the heart's surface is compared with measured speed of propagation along the surface. Since it is reasonable to assume no currents go out of the myocardium, the wave front of the action potential can be considered to be travelling along the surface. That is, a Neumann boundary condition is typically used so that, close to the surface, the 2D speed vector along the surface and the 3D wavefront speed vector should be very similar.

Preliminary results for adjusting a surface model using contact mapping measurements were obtained in Moreau-Villeger et al. (2006). We extend this work here by using the data obtained from optical recordings, mapped on to the surface and registered with the 3D volumetric mesh (obtained from MRI) as described earlier. First, we define the model initial conditions based on the onset of the electrical propagation. The excitation area is defined automatically by finding the vertices corresponding to the local minima of the depolarization times and their direct neighbors. We compared the vertices coordinates where the excitation area started with the marker coordinates (which gave precise location of the electrode tip in the optical image) and were found to be within 0.5 cm apart. We then find a physiological range of parameter values to best represent the data. For this, we analyze the histogram of the conduction velocity in the measurements obtained (described later in Section 3, Fig. 11b). In order to increase the robustness of the method and speed up the optimization, the ventricles are divided into regions where the parameters are constant within a region. The left ventricle is therefore divided into 17 regions as defined by the American Heart Association (Cerqueira et al., 2002) and a similar division is applied to the right ventricle, resulting in 26 regions in total. To achieve an automatic adjustment of the local conductivity (per region) in the model based on the measured isochrones, it is important to obtain a good initialization. Thus, the quantitative adjustment of the model to the data is done in two steps. First, an automatic initialization step provides a value of d_i for each region of the model; then an iterative gradient descent algorithm is used to decrease the error in the speed for each region.

To achieve this initialization, we look for an analytical relationship between the conductivity and the speed. This function can then be used to initialize the minimization in each region. From a one-dimensional analysis of the Aliev and Panfilov model, it was shown (Keener and Sneyd, 1998; Moreau-Villeger et al., 2006) that planar waves are solutions of the following equation, yielding a relationship between the speed of the depolarization front (i.e., the conduction velocity) c in stationary mode and the parameters k and d:

$$c = \sqrt{2 \cdot k \cdot d}(0.5 - a). \tag{3}$$

Although this formula is only true in one dimension (since, in the case of two- or three-dimensional propagations, the curvature of the diffusion front affects its velocity), the relation can still indicate approximately the c–d dependence.

The initialization method involves simulating several propagations on the mesh using different values of d and characterizing the corresponding median velocities within each region; we ensure that this range of c includes the measured velocities. We then fit the following function to these (c, d) data pairs based on the one-dimensional formula (Eq. (3)):

$$c(d) = \alpha \cdot \sqrt{d} + \beta, \tag{4}$$

estimating the parameters α and β by minimizing mean squared error (Fig. 12).

Once α and β in Eq. (4) are estimated, we can initialize as follows the value of d_i for each region from the mean conduction velocity, $\bar{c}_i$, of that region computed with the measured activation times:

$$d_i = \left(\frac{\bar{c}_i - \beta}{\alpha}\right)^2. \tag{5}$$

The *iterative adjustment* of the model is described next. After the initialization of the pseudo-conductivity d, we try to iteratively improve the model fitting. We chose a simple gradient descent algorithm as the optimization method. We minimize the following criterion in each region: $J(d_i) = (\bar{c}_i - \hat{c}_i(d_i))^2$ where $\hat{c}_i(d_i)$ is the mean of the simulated velocity in a given region for the parameter value d_i. We further calculate the local derivative of the criterion by centered finite differences, which require solving two forward problems at each iteration in addition to performing a simulation after each iteration to update the value of the criterion.

By minimizing the differences between the simulated and measured velocities for each region instead of using the depolarization times, we allow adjustment of all the regions at the same time and thus considerably reduce the number of simulations needed to compute the gradient descent algorithm. Indeed, compared to using the depolarization times where there is a strong causality and for which a variation of conductivity of a region upstream affects all the following regions, we are able to simplify the problem recognizing that the conduction velocity at a given position depend only on the conductivity at that position. In other words, all the parameters converge independently to the minima of their respective criterion.

3. Results

3.1. Building the theoretical model

Fig. 4 shows the steps involved in the construction of the model (in one of the hearts). The computational model is first obtained from anatomical images (Fig. 4a); the fiber directions (obtained from diffusion-weighted MR images) are then specified at the baricenter of each tetrahedral element of the mesh (Fig. 4b). The fiber directions can be visualized using MedINRIA[1] software (Fig. 4c), which encodes the RGB colors for the three orthogonal directions associated with fiber orientation. Following expectations, the fiber

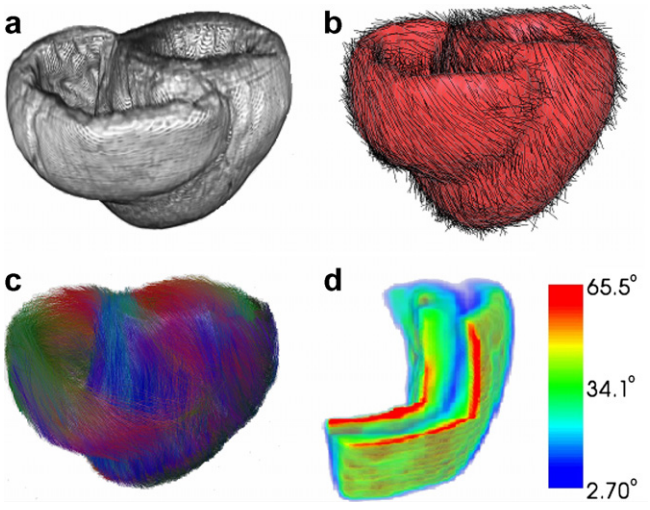

Fig. 4. The heart model from anatomy images (a), with fiber orientation assigned at each vertex (b). Fiber orientation (c) displayed using MedINRIA software; the fiber angle varying from epicardium to endocardium viewed through the ventricle (d).

angle changes from the epicardium to the endocardium, as shown in Fig. 4d (plotted using Matlab).

3.2. 3D stereo reconstruction of epicardial surface and registration with the MR surface

Results from the 3D stereo reconstruction are presented in Fig. 5, where, for example a 3D optical image of the heart was texture mapped onto the reconstructed 3D optical surface. For the optical imaging configuration used to generate the results shown in this paper, the 3D reconstruction procedure was able to measure the depth of an image point to within 2 mm, and its fronto-parallel position to within 0.5 mm. A small (approximately 2 pixels) lateral margin of the heart cannot be reconstructed with accuracy, as this area falls out of the two (left and right) views.

The stimulating electrode location (Fig. 6a) from one of the sites where the heart was paced, is given by the marker encircled in the 2D optical image in Fig. 6b. Fig. 6c shows the markers visible in MR images.

After the computed rigid transformation aligning MR and optical datasets, the 3D coordinates of the markers determined by optical stereo reconstruction were in general estimated to be less than 3 mm from their positions indicated in the volumetric MR scan for the five hearts on which registration was performed (see an example in Fig. 7a).

An example of the stereo surface (with the image of the markers textured onto it) following registration with the mesh is presented in Fig. 7b. Note that such estimations were performed for four other hearts and the distances were consistently found to be within 3 mm (see Table 1).

3.3. Comparison between computer simulation and experiments

Fig. 8 displays a qualitative comparison between 2D optical images (a–d) and simulation results (for anisotropic and isotropic cases) of the action potential propagation at a few instances in time (depolarized phase in red and the repolarized state in blue). The activation propagates from the stimulation point close to the apex, toward the base, faster in the direction parallel to the fibers, as can be noticed from the comparison between the anisotropic (e–h) and isotropic cases (i–l). Note that a good agreement was found in all hearts when we qualitatively compared the recorded propagation with simulations.

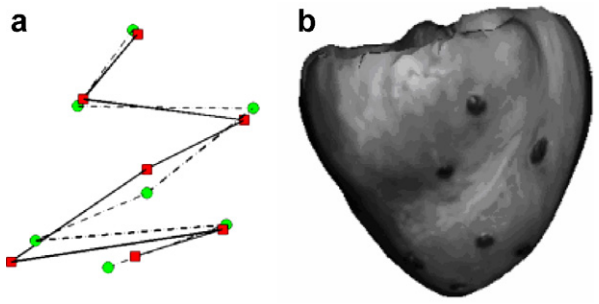

Fig. 7. (a) Results of rigid transformation (after rotation, scaling and translation) with green dots representing markers in optical images and red dots representing the markers in MR images); (b) the 3D stereo surface after texture mapping of the markers' image, and further registered with the volumetric mesh. (For interpretation of the references to color in this figure legend, the reader is referred to the web version of this article.)

3.4. Analysis of action potential waves

Fig. 9a shows how we analyze the signal to derive APD90. The restitution curve of APD90 (i.e., the dependence of action potential duration on pacing frequency or equivalently the inverse of cycle length CL) relates the APD of one cycle (n) to the diastolic interval D.I. of the preceding cycle ($n-1$). Under steady-state pacing protocols, this relation: $APD_n = f(CL - APD_{n-1})$ exhibits an exponential behavior. One heart (i.e., #4) was paced at steady-state frequencies (from 0.5 to 2 Hz), for which the APD90 was derived. Fig. 9b shows a comparison between measured, and simulated restitution curve.

3.5. Isochronal maps

The activation times can also be represented by isochronal lines connecting pixels of equal activation time, as well as by color maps representing depolarization times over one heart cycle. The propagation follows the fiber directions and depends on the stimulation site. Examples of experimental isochronal contours and color maps

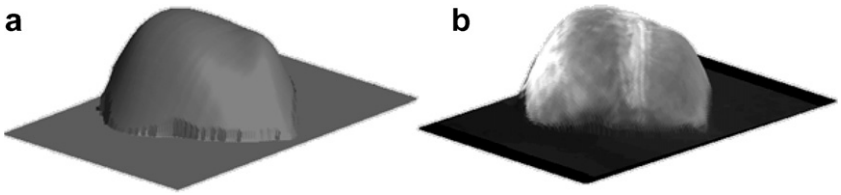

Fig. 5. Results from the 3D stereo reconstruction: (a) surface rendering and (b) and texture mapping onto the 3D reconstructed surface.

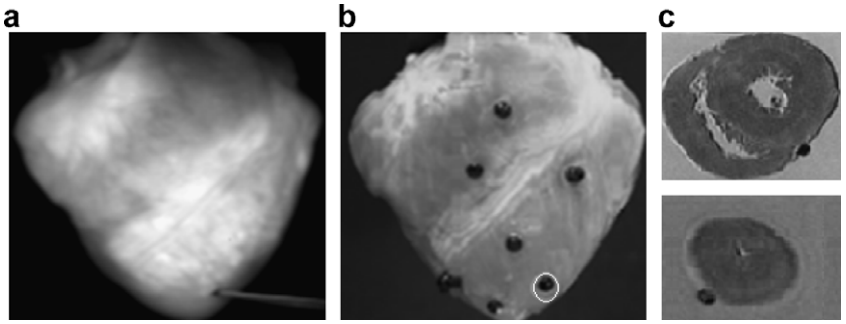

Fig. 6. (a) The electrode position, (b) the markers locations in optical image under normal lighting and (c) markers visible in MR images, respectively.

Please cite this article in press as: Pop, M. et al., Fusion of optical imaging and MRI for the evaluation and adjustment ..., Med. Image Anal. (2008), doi:10.1016/j.media.2008.07.002

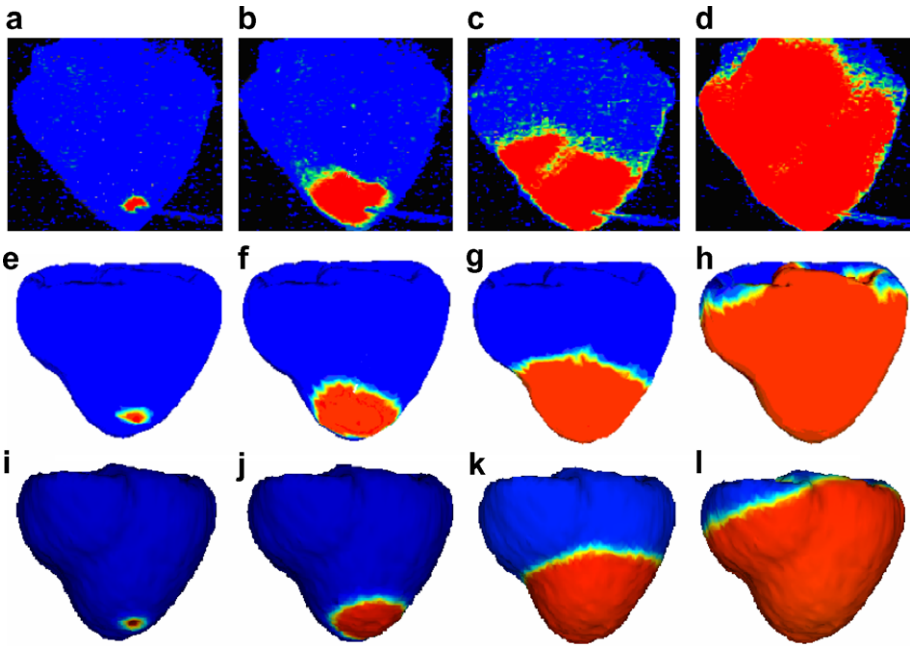

Fig. 8. Qualitative comparison of the AP propagation. Snapshots at different time instances: (a–d) 2D optical recordings, (e–h) 3D theoretical predictions for anisotropic case, and (i–l) 3D theoretical propagations in isotropic case.

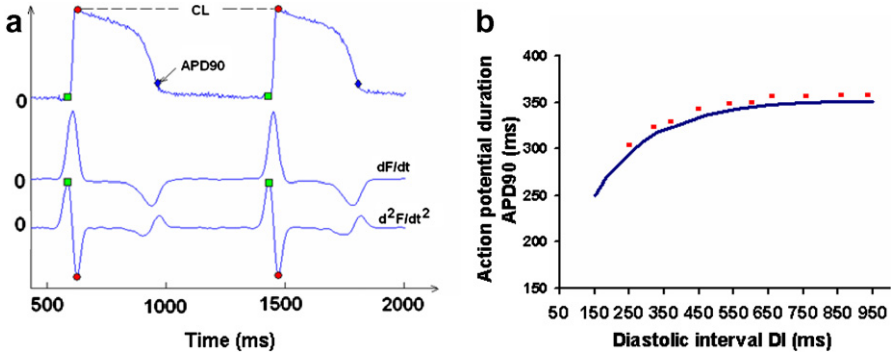

Fig. 9. (a) Analysis of AP wave using the derivatives of the signal and (b) restitution curves (experimental data points shown as circles, in good agreement with the simulated curves shown as line).

(from heart #5) are presented in Fig. 10. Various data sets correspond to recordings obtained from placement of the stimulating electrode at four different positions: outside (a and c) and inside (b) of the LV; and inside (d) the RV. For clarity, the exact pacing locations are given in Fig. 10e–h. The contour lines corresponding to the 2D optical recordings in the isochrones are displayed 10 ms apart in Fig. 10a–d, whereas in Fig. 10i–l, we can observe the experimental color isochrones after texture mapping onto the 3D mesh.

3.6. Quantitative adjustment of the electrophysiology model

The initial mean error in depolarization times at the vertices when simulating the propagation using literature values for the model parameters is 28.9 ms. From the measured depolarization times (Fig. 11a), we first compute conduction velocity (see an example in Fig. 11b). A histogram of the conduction velocity at each position is shown in Fig. 11c. As expected in the myocardium, the mean value is around 40 cm/s (lower due to the anisotropy). To proceed with model adjustment to reduce errors, the vertices corresponding to the electrical onset (pacing position) were detected and the mesh divided into regions as described in Section 2.3.1.

The initialization function (Eq. (4)) for model adjustment relating conduction velocity to d was estimated from (c,d) data pairs determined by simulations performed over a range of pseudo-conductivities, as plotted in Fig. 12. The figure presents points for 10 simulations using 10 different values of d, and computing the 10 resulting mean velocities. The estimated function yields a very good fit to the calculated (c,d) pairs. Thus at the global scale, the relationship appears to be usable. This step was only designed to initialize the gradient descent in each region, as curvature will change this relationship. However, in fact this step does the major part of the adjustment, probably because the wavefront is relatively flat in many regions.

Finally, the gradient descent algorithm is used to improve the model fitting; the evolution of errors in selected regions is presented in Fig. 13. Specifically, it shows the evolution of the error for five different regions in one heart: step −1 shows the error before any model adjustment; step 0 is after initialization; we then see results from four steps of gradient descent. For each case, the

Please cite this article in press as: Pop, M. et al., Fusion of optical imaging and MRI for the evaluation and adjustment ..., Med. Image Anal. (2008), doi:10.1016/j.media.2008.07.002

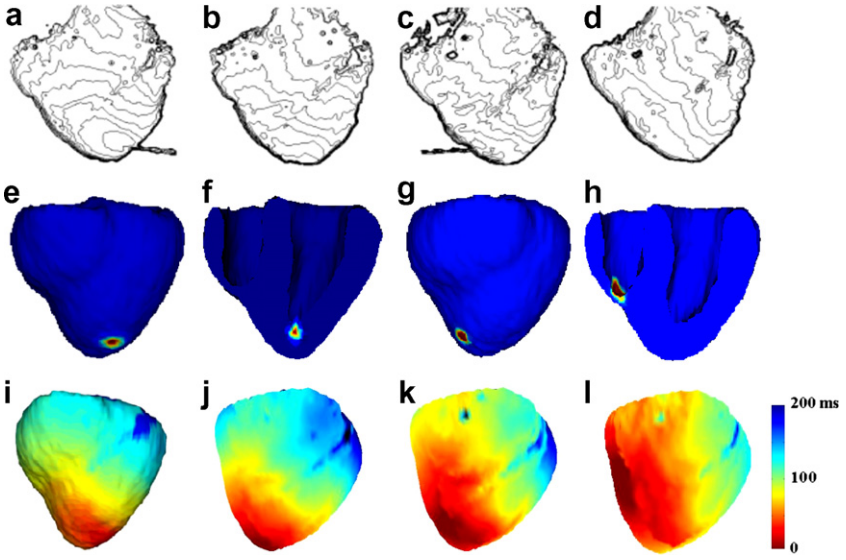

Fig. 10. Isochronal maps from placing the electrode at different sites on the heart: (a–e) isochronal lines obtained in 2D optical images; (e–h) exact pacing locations (in red); (i–l) color isochrones texture mapped onto the 3D mesh. (For interpretation of the references to color in this figure legend, the reader is referred to the web version of this article.)

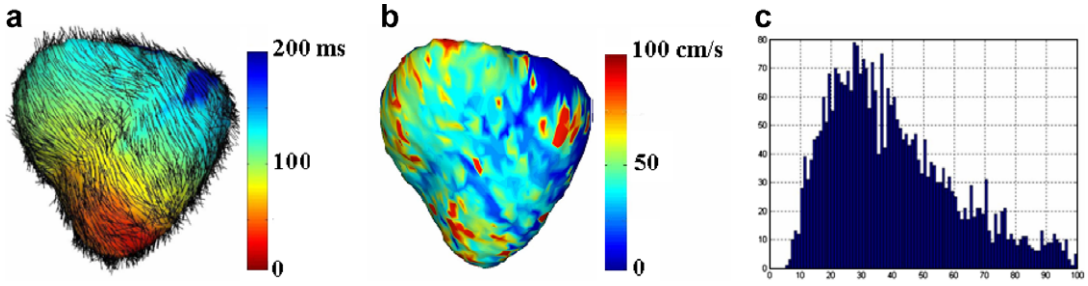

Fig. 11. (a) Measured depolarization isochrones (ms) shown on a mesh with fibers, (b) map of conduction velocities (cm/s) computed from depolarization times, and (c) histogram of the measured conduction velocities (cm/s).

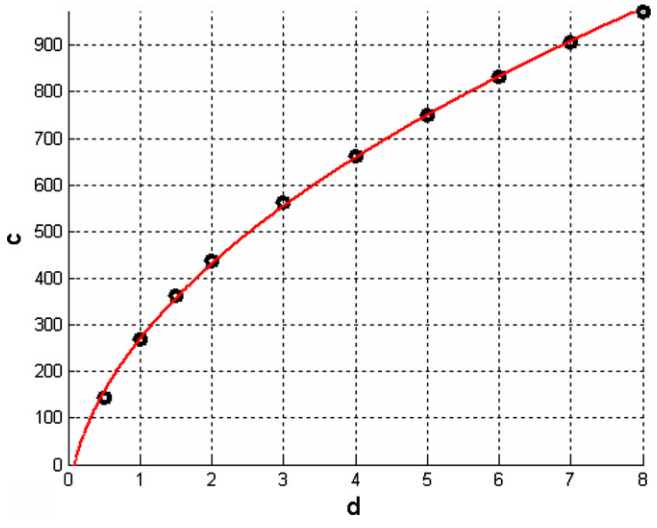

Fig. 12. Estimated analytical relationship between d and the conduction velocity c (mm/s). Black dots represent results from the simulations on a range of parameters, and the red curve is the estimated function. (For interpretation of the references to color in this figure legend, the reader is referred to the web version of this article.)

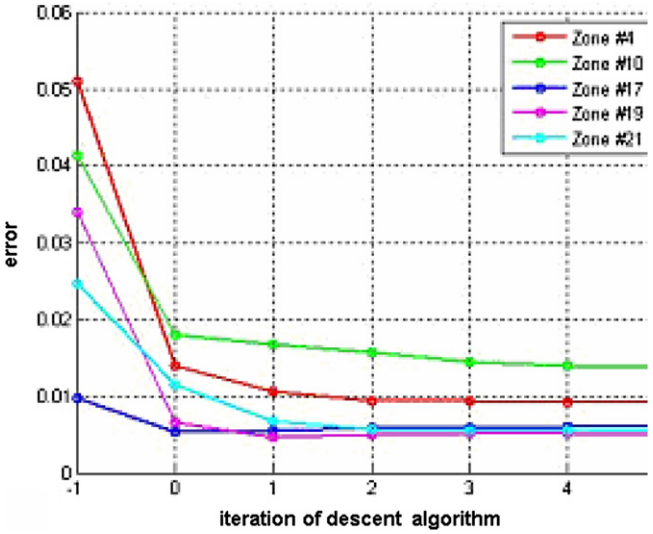

Fig. 13. Evolution of errors on depolarization times (in s) in five different regions of the heart.

error is the mean absolute difference between depolarization times predicted by the model vs. measured in the experiment, averaged across vertices within that region.

Fig. 14 shows the depolarization isochrones, including the reference (measured time), as well as the isochronal maps before and after adjustments.

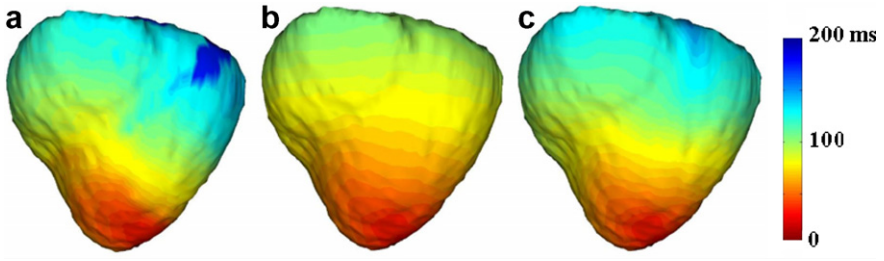

Fig. 14. Depolarization isochrones: (a) reference (measured times); (b) predicted initial times before adjustment; (c) predicted times after n iterations of adjustment (the times in the color bar are in ms). (For interpretation of the references to color in this figure legend, the reader is referred to the web version of this article.)

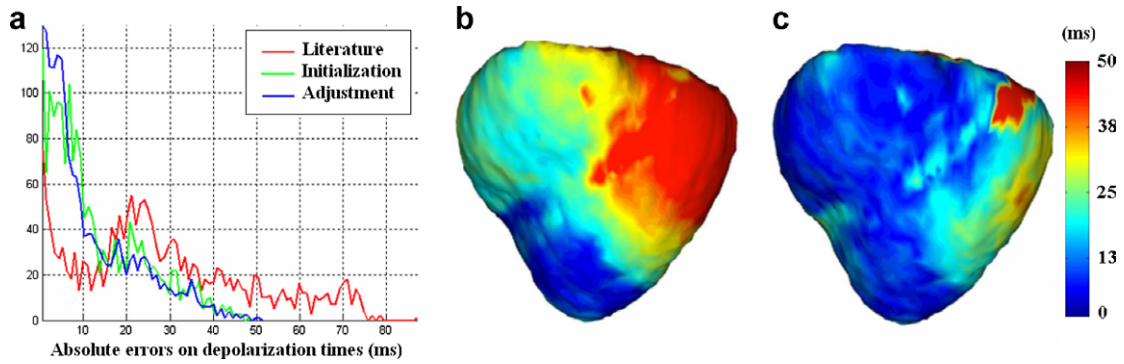

Fig. 15. (a) Histogram of errors on depolarization times across vertices: the red curve represents the initial errors, the green curve after initialization and the blue curve after gradient descent; (b) map of the error before adjustment; (c) map of the error after adjustment (in ms). (For interpretation of the references to color in this figure legend, the reader is referred to the web version of this article.)

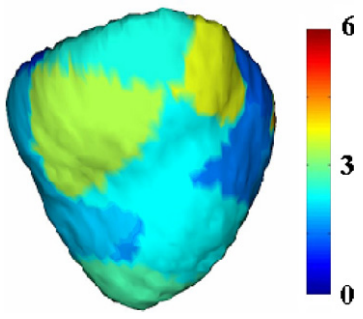

Fig. 16. Values of pseudo-conductivity d after adjustment for each of the visible regions.

The initialization provides a robust method to estimate the relationship between the apparent conductivity and the propagation velocity, taking into account the approximation of the discretisation. It yields a drastic decrease of the mean error in depolarization times across regions (from 28.9 to 13.1 ms). The gradient descent algorithm yields further improvement reducing the mean error to 11.7 ms (see histogram and maps of errors in Fig. 15).

The resulting conductivity map (Fig. 16) is rather homogeneous as would be expected for a healthy heart. Note that the patchiness reflects the discretization of the values of d into regions. Diminished conductivity in the territory of the left anterior descending artery might by explained by reduced perfusion to this region in the experimental set-up which potentially resulted in an ischemic area, causing the wave to propagate slower.

4. Discussion and future work

In the work presented here, we propose a method to compare and adjust a macroscopic model of electrophysiology with measurements in an *ex vivo* model of healthy porcine hearts, and have presented preliminary results. For this, we used measurements of action potential obtained from optical fluorescence images, together with the anatomy and fiber directions obtained via MR imaging. Our first task was to compare the predictions of the mathematical model with direct measurements of action potential in healthy hearts, validating the basic model; a second step was to use this information to adjust model parameters for better correspondence. The AP duration and propagation is measured with high spatial (i.e., 0.7-mm) and temporal (i.e., 3.7 ms) resolution via optical imaging, which allowed us to observe the AP wave in detail. The computer model was then built from MR anatomical images of the same heart, and integrated with information on structural anisotropy from MR measurement of fiber directions. The main output of the model is the solution for transmembrane potential, from which we can further analyze the AP propagation and the isochronal maps. The heart was paced at different locations and the wave propagated, as expected, about twice as fast in the direction along the fiber compared to the orthogonal (transverse) direction.

Moreover, to realistically compare simulated and measured activation maps, we have developed a novel 3D stereo reconstruction of the heart surface. This reconstruction was further registered with the mesh to be able to compare accurately the activation times in experiments and simulations; the rigid registration between the optical and MR surfaces based on limited marker positions yielded excellent correspondence (i.e., the markers' coordinates in the optical and the MRI datasets generally corresponded to less than 3 mm). We acknowledge that the surface reconstructed using stereoscopic methods only covers about half of the heart, but a very few rotations of the heart (i.e., a total of three) in front of the cameras should be enough to fully recover the 3D surface of the myocardium. Current work is being done in our laboratory to develop such a device and experiments are under way to complete this task.

Please cite this article in press as: Pop, M. et al., Fusion of optical imaging and MRI for the evaluation and adjustment ..., Med. Image Anal. (2008), doi:10.1016/j.media.2008.07.002

Improvements could be made to decrease the final error between model predictions and experimental measurements of conduction velocity. One issue is the region of integration corresponding to the optical measurements. The epicardial optical signals contain a depth-weighted average of transmembrane potential signals generated by the fluorescent photons from a 3D volume beneath the surface (Hyatt et al.,2005; Bishop et al., 2006). In the current work, we limited comparison of experimental measures to the solution of the Aliev and Panfilov model at the epicardial surface, with good correspondence. We acknowledge that, correcting the simulated voltages as well as better interpretation of the optical up-stroke shapes as per the methods provided in these papers aforementioned could improve the quality of the correspondence between our measurements and calculations. Other recent studies (Hillman et al., 2007) showed that electrical propagation in rat hearts can be mapped using depth-resolved optical imaging; however, due to the thickness of the pig ventricle such technique is not feasible in our experiments.

Although the macroscopic Aliev and Panfilov model is simple compared to ionic and bidomain models, it is feasible to computations on large hearts. The model behavior was very good given the initialization of parameters using literature data obtained from dog data (as obtained from qualitative comparisons of simulated and measured activation maps as well as restitution curves). Further, the error (initially 30 ms) after adjustment can be reduced by a factor of three, with a final mean error of around 10 ms for a depolarization time which is between 0 and 200 ms. This is a good result given the small number of parameters (only 26 regions for the whole myocardium). As means of improving correspondence between model and experiment, a multi-resolution scheme with region decomposition in the estimation of d_i values would help in convergence and provide finer correction in regions where the conductivity varies substantially. That said, the adjustment process gave good preliminary results considering the macroscopic aspect of the model, while yielding a reasonable computational time. Finer adjustment may be more important when characterizing pathology. At issue in a clinical scenario, would be to predict, for instance the cycle length in ventricular tachycardia, VT. Thus, a reduction in initial error of 30 ms (obtained from data collected during the electrophysiology study) would definitely improve the accuracy of the cycle length predictions.

The measured isochronal maps had an expected general pattern, directly related to a faster conduction velocity along the fibers and agreed well with simulated maps in all hearts (although we illustrated examples only from the heart used to perform the adjustment). However, as a second consideration, smoothing the DTI data in order to obtain a better representation of continuous fibers could give a better fit. Indeed, the longitudinal propagation speed seems to be slower in the simulation than in the experiment, potentially due to some discontinuities in the fiber orientations obtained from reconstruction. On a related issue, we are currently testing a model based on synthetic fibers extrapolated from population data sets. For the *in vivo* situation, it would be much easier to use such prior knowledge of typical fiber directions; so far results we have obtained with synthetic fibers are similar at least for this healthy case.

It is generally known that in structurally diseased hearts, the wave propagation is abnormal and vulnerable to reentry phenomena as reviewed by Kleber and Rudy (2004), which gives rise to ventricular tachycardia, potentially degenerating into fibrillation. In future studies, we therefore plan to test the computer model by performing simulations studying the perturbation in the wave propagation in the presence of such anatomic blocks and areas of slow electrical conduction in an infarct model. Other optical studies (in small hearts) demonstrated that the optical technique is feasible to map epicardial macro-reentrant circuits (Girouard and Rosenbaum, 2001; Pastore and Rosenbaum, 2000) associated with structural barriers. Our set-up is appropriate for similar studies in large hearts and allows for further testing and adjustment of the computer model. Thus, our next task will be to predict the electrical propagation in certain pathologic cases, for which MRI will provide not only the fiber directions (to study the interaction of local anisotropy and impulse propagation) but also anatomical and structural information. MRI is known to be a powerful tool used to finely characterize infarct heterogeneities associated with macro-reentrant VT (Ashikaga et al., 2007).

Nevertheless, the final step will be the translation of this work and application of fast models into clinical studies. To do so, we need to be able to obtain similar surfacic data (i.e., during the electrophysiology study) and register them with a 3D volumetric model. For example, the adjustments might be performed using maps from available diagnostic tools such as the Ensite and CARTO systems, registered to MRI data sets although information about fiber orientation will be limited in such studies, as *in vivo* DTI does not yield sufficiently spatial resolution (Wu et al., 2006).

5. Conclusion

In this work, we have provided an evaluation and adjustment method of a macroscopic model of cardiac electrophysiology. Specifically, we have compared the output of the theoretical model (based on Aliev–Panfilov macroscopic formalism) calibrated with MRI data depicting anatomy and fiber orientations, with measurements of AP obtained using an optical imaging technique in an *ex vivo* preparation of large, healthy porcine hearts. Further analysis of AP wave characteristics and the speed of the propagation of the depolarization wavefront can be used to adjust the input model parameters (i.e., the conductivity).

Acknowledgments

The authors would like to thank Dr. J.M. Rogers (University of Alabama, Birmingham, USA) for valuable discussions regarding the optical technique, Dr. P. Helm (University of Virginia, USA) for help with implementing the diffusion-weighted sequence on our scanner and to Mr. Jean-Marc Peyrat for his help with visualization of fibers orientation. We are also grateful to Mr. D. Chung and Mr. G. Liu for initial software development and technical assistance with the optical set-up as well as to the veterinary technicians at Sunnybrook for help with the animal studies. We also thank Mrs. Y. Dalal for assistance in manuscript preparation. This study was supported by funding from the Canadian Institutes of Health Research (Grant Number MOP36477), Ontario Research and Development Challenge Fund, the Canadian Foundation for Innovation, and the Ontario Innovation Trust. Ms. Mihaela Pop was supported by a Ph.D. scholarship from the Heart and Stroke Foundation of Canada.

References

Aliev, R.R., Panfilov, A.V., 1996a. Modeling of heart excitation patterns caused by a local inhomogeneity. Journal of Theoretical Biology 181, 33–40.

Aliev, R.R., Panfilov, A.V., 1996b. A simple two-variable model of cardiac excitation. Chaos, Solitons and Fractals 7, 293–301.

Ashikaga, H., Sasano, T., Dong, J., Zviman, M.M., Evers, R., Hopenfeld, B., Castro, V., Helm, R.H., Dickfeld, T., Nazarian, S., Donahue, J.K., Berger, R.D., Calkins, H., Abraham, M.R., Marbn, E., Lardo, A.C., McVeigh, E.R., Halperin, H.R., 2007. Magnetic resonance-based anatomical analysis of scar-related ventricular tachycardia: implications for catheter ablation. Circulation Research 101 (9), 939–947.

Banville, I., Gray, R.A., 2002. Effect of action potential duration and conduction velocity restitution and their spatial dispersion on alternans and the stability of arrhythmias. Journal of Cardiovascular Electrophysiology 13, 1141–1149.

Bayly, P.V., KenKnight, B.H., Rogers, J.M., Hillsley, R.E., Ideker, R.E., Smith, W.M., 1998. Estimation of conduction velocity vector fields from epicardial mapping data. IEEE Transactions on Biomedical Engineering 45, 563–571.

Bishop, M.J., Rodriguez, B., Eason, J., Whiteley, J.P., Trayanova, N., Gavaghan, D.J., 2006. Synthesis of voltage-sensitive optical signals: application to panoramic optical mapping. Biophysical Journal 90, 2938–2945.

Cerqueira, M.D., Weissman, N.J., Dilsizian, V., Jacobs, A.K., Kaul, S., Laskey, W.K., Pennell, D.J., Rumberger, J.A., Ryan, T., Verani, M.S., 2002. Standardized myocardial segmentation and nomenclature for tomographic imaging of the heart: a statement for healthcare professionals from the Cardiac Imaging Committee of the Council on Clinical Cardiology of the American Heart Association. Circulation 105, 539–542.

Chung, D., Pop, M., Sermesant, M., Wright, G.A., 2006. Stereo reconstruction of the epicardium for optical fluorescence imaging. In: Esboll, B.J., Jorgensen, T.M. (Eds.), MICCAI Workshop on Biophotonics for Diagnosis and Treatment, pp. 33–40.

Ciaccio, E.J., Lee, T., 2002. Isochronal difference mapping: an approach for mapping dynamic changes during reentrant ventricular tachycardia. Pace-Pacing and Clinical Electrophysiology 25, 1737–1746.

Clayton, R.H., Holden, A.V., 2004. Propagation of normal beats and re-entry in a computational model of ventricular cardiac tissue with regional differences in action potential shape and duration. Progress in Biophysics and Molecular Biology 85, 473–499.

Clayton, R.H., Holden, A.V., 2005. Dispersion of cardiac action potential duration and the initiation of re-entry: a computational study. Biomedical Engineering Online 4, 11.

Efimov, I.R., Huang, T.D., Rendt, J.M., Salama, G., 1994. Optical mapping of repolarization and refractoriness from intact heart. Circulation Research 90, 1469–1480.

Efimov, I.R., Nikolski, V.P., Salama, G., 2004. Optical imaging of the heart. Circulation Research 95, 21–33.

Eldar, M., Ohad, D.G., Goldberger, J.J., Rotstein, Z., Hsu, S., Swanson, D.K., Greenspon, A.J., 1997. Transcutaneous multielectrode basket catheter for endocardial mapping and ablation of ventricular tachycardia in the pig. Circulation 96 (7), 2430–2437.

Elharrar, V., Surawicz, B., 1983. Cycle length effect on restitution of action potential duration in dog cardiac fibers. The American Journal of Physiology 244, H782–H792.

Faris, O.P., Evans, F.J., Ennis, D.B., Helm, P.A., Tylor, J.L., Chesnick, A.S., Guttman, M.A., Ozturk, C., McVeigh, E.R., 2003. Novel technique for cardiac electro-mechanical mapping with MRI tagging and epicardial sock. American Journal of Physiology: Heart and Circulatory Physiology 285 (5), H1864–H1870.

Girouard, S.D., Rosenbaum, D.S., 2001. Role of wavelength adaptation in the initiation, maintenance, and pharmacologic suppression of reentry. Journal of Cardiovascular Electrophysiology 12 (6), 697–707.

Hao, S.C., Christini, D.J., Stein, K.M., Jordan, P.N., Iwai, S., Bramwell, O., Markowitz, S.M., Mittal, S., Lerman, B.B., 2004. Effect of beta-adrenergic blockade on dynamic electrical restitution in vivo. American Journal of Physiology 287, H390–H394.

Helm, P.A., Tseng, H.J., Younes, L., McVeigh, E.R., Winslow, R.L., 2005. *Ex vivo* 3D diffusion tensor imaging and quantification of cardiac laminar structure. Magnetic Resonance in Medicine 54, 850–859.

Hillman, E.M.C., Bernus, O., Pease, E., Bouchard, M.B., Pertsov, A., 2007. Depth-resolved optical imaging of transmural electrical propagation in perfused heart. Optics Express 15, 17827–17841.

Horn, B.K.P., 1987. Closed-form solution of absolute orientation using unit quaternions. Journal of the Optical Society of America A 4, 629–642.

Hyatt, C.J., Mironov, S.F., Vetter, F.J., Zemlin, C.W., Pertsov, A.M., 2005. Optical action potential upstroke morphology reveals near-surface transmural propagation direction. Circulation Research 97, 277–284.

Kadish, A., Shinnar, M., Moore, E.N., Levine, J.H., Balke, C.W., Spear, J.F., 1988. Interaction of fiber orientation and direction of impulse propagation with anatomic barriers in anisotropic canine myocardium. Circulation 78, 1478–1494.

Kay, M.W., Amison, P.M., Rogers, J.M., 2004. Three-dimensional surface reconstruction and panoramic optical mapping of large hearts. IEEE Transactions on Biomedical Engineering 51, 1219–1229.

Keener, J.P., Sneyd, J., 1998. Mathematical Physiology. Springer.

Kim, B.S., Kim, Y.H., Hwang, G.S., Pak, H.N., Lee, S.C., Shim, W.J., Oh, D.J., Ro, Y.M., 2002. Action potential duration restitution kinetics in human atrial fibrillation. Journal of the American College of Cardiology 39, 1329–1336.

Kleber, A.G., Rudy, Y., 2004. Basic mechanisms of cardiac impulse propagation and associated arrhythmias. Physiological Reviews 84, 431–488.

Moreau-Villeger, V., Delingette, H., Sermesant, M., Ashikaga, H., McVeigh, E., Ayache, N., 2006. Building maps of local apparent conductivity of the epicardium with a 2D electrophysiological model of the heart. IEEE Transactions on Biomedical Engineering 53, 1457–1466.

Nanthakumar, K., Jalife, J., Masse, S., Downar, E., Pop, M., Asta, J., Ross, H., Rao, V., Mironov, S., Sevaptsidis, E., Rogers, J., Wright, G., Dhopeshwarkar, R., 2007. Optical mapping of Langendorff-perfused human hearts: establishing a model for the study of ventricular fibrillation in humans. American Journal of Physiology: Heart and Circulatory Physiology 293, H875–H880.

Nash, M.P., Panfilov, A.V., 2004. Electromechanical model of excitable tissue to study reentrant cardiac arrhythmias. Progress in Biophysics and Molecular Biology 85, 501–522.

Pastore, J.M., Rosenbaum, D.S., 2000. Role of structural barriers in the mechanism of alternans-induced reentry. Circulation Research 87, 1157–1163.

Qin, H., Kay, M.W., Chattipakon, N., Redden, D.T., Ideker, R.E., Rogers, J.M., 2003. Effects of heart isolation, voltage-sensitive dye, and electromechanical uncoupling agents on ventricular fibrillation. American Journal of Physiology: Heart and Circulatory Physiology 284, H1818–H1826.

Schmitt, C., Zrenner, B., Schneider, M., Karch, M., Ndrepepa, G., Deisenhofer, I., Weyerbrock, S., Schreieck, J., Schomig, A., 1999. Clinical experience with a novel multielectrode basket catheter in right atrial tachycardias. Circulation 99 (18), 2414–2422.

Sermesant, M., Faris, O., Evans, F., McVeigh, E., Coudiere, Y., Delingette, H., Ayache, N., 2003. Preliminary validation using in vivo measures of a macroscopic electrical model of the heart. Surgery Simulation and Soft Tissue Modelling. Springer, Berlin/Heidelberg.

Sermesant, M., Rhode, K., Sanchez-Ortiz, G.I., Camara, O., Andriantsimiavona, R., Hegde, S., Rueckert, D., Lambiase, P., Bucknall, C., Rosenthal, E., Delingette, H., Hill, D.L., Ayache, N., Razavi, R., 2005. Simulation of cardiac pathologies using an electromechanical biventricular model and XMR interventional imaging. Medical Image Analysis 9, 467–480.

Sermesant, M., Delingette, H., Ayache, N., 2006. An electromechanical model of the heart for image analysis and simulation. IEEE Transactions on Medical Imaging 25, 612–625.

Sung, D., Omens, J.H., McCulloch, A.D., 2000. Model-based analysis of optically mapped epicardial activation patterns and conduction velocity. Annals of Biomedical Engineering 28, 1085–1092.

Taccardi, B., Punske, B.B., Macchi, E., Macleod, R.S., Ershler, P.R., 2008. Epicardial and intramural excitation during ventricular pacing: effect of myocardial structure. American Journal of Physiology: Heart and Circulatory Physiology 294 (4), H1753–H1766.

Vetter, F.J., Simons, S.B., Mironov, S., Hyatt, C.J., Pertsov, A.M., 2005. Epicardial fiber organization in swine right ventricle and its impact on propagation. Circulation Research 96, 244–251.

Wu, M.T., Tseng, W.Y.I., Su, M.Y.M., Liu, C.P., Chiou, K.R., Wedeen, V.J., Reese, T.G., Yang, C.F., 2006. Diffusion tensor magnetic resonance imaging mapping the fiber architecture remodeling in human myocardium after infarction – correlation with viability and wall motion. Circulation 114, 1036–1045.

Yang, Z., Zhang, H., Kong, S., Yue, X.F., Jin, Y.B., Jin, J., Huang, Y.C., 2007. Study for relevance of the acute myocardial ischemia to arrhythmia by the optical mapping method. Physiological Measurement 28, 481–488.

Please cite this article in press as: Pop, M. et al., Fusion of optical imaging and MRI for the evaluation and adjustment ..., Med. Image Anal. (2008), doi:10.1016/j.media.2008.07.002